Letters

Sequence-Impedance-Based Stability Comparison Between VSGs and Traditional Grid-Connected Inverters

Wenhua Wu, *Student Member, IEEE*, Leming Zhou, *Member, IEEE*, Yandong Chen, *Member, IEEE*, An Luo, *Senior Member, IEEE*, Yanting Dong, Xiaoping Zhou, *Student Member, IEEE*, Qianming Xu, *Member, IEEE*, Ling Yang, *Student Member, IEEE*, and Josep M. Guerrero, *Fellow, IEEE*

***Abstract*—Traditional grid-connected inverters (TGCI) could suffer from small-signal instability owing to the dynamic interactions among inverters and a weak grid. In this letter, the small-signal sequence impedance model of the virtual synchronous generator (VSG) is built, and the sequence impedance characteristics of the VSG and the TGCI are compared and analyzed. The sequence impedance of the TGCI is mainly capacitive in the middle-frequency area, and the impedance amplitude is quite high. By contrast, the sequence impedance of the VSG, being consistent with the grid impedance characteristics, is generally inductive, and the impedance amplitude is quite low. Based on the sequence impedance model and the Nyquist stability criterion, the influence of the grid stiffness, the number of paralleled inverters, and the phase-locked loop (PLL) bandwidth on the stability of the VSG and the TGCI systems is analyzed. The stability analysis results show that the TGCI loses stability easily, whereas the VSG still works well without PLL restrictions under an ultraweak grid or with a large number of inverters connected to the grid. Therefore, the VSG is more suitable than the TGCI for achieving high penetration of renewable energy generation in an ultraweak grid from a system stability viewpoint. Finally, the experimental results validate the sequence impedance model and the stability analysis.**

***Index Terms*—Harmonic oscillation, sequence impedance modeling, ultraweak grid, virtual synchronous generator (VSG).**

I. Introduction

IN RECENT years, renewable energy generation has developed rapidly, owing to the increasing fossil fuel shortage and

Manuscript received March 15, 2018; revised April 25, 2018; accepted May 17, 2018. Date of publication May 27, 2018; date of current version November 19, 2018. This work was supported in part by the National Key Research and Development Program of China under Grant 2017YFB0902000, in part by the State Grid Science and Technology Project under Grant SGXJ0000KXJS1700841, and in part by the Natural Science Foundation of China under Grant 51577056. *(Corresponding author: Leming Zhou.)*

W. Wu, L. Zhou, Y. Chen, A. Luo, X. Zhou, Q. Xu, and L. Yang are with the College of Electrical and Information Engineering, Hunan University, Changsha 410082, China (e-mail:

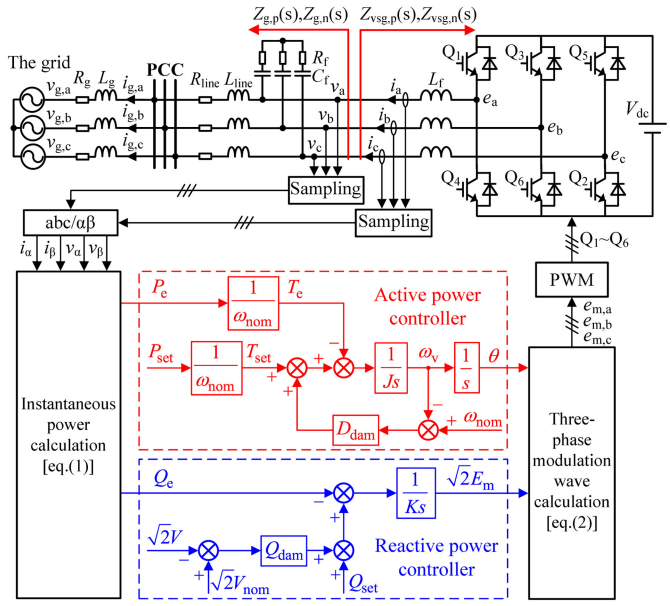

Fig. 1. Topology and control scheme of the VSG.

in SRRFs [12] or in SRFs [8]. When the VSG is controlled in SRFs, its output voltage and current are alternating time variables with no dc-operation point. Therefore, it is difficult to apply the traditional time-domain linearization method to the VSG controlled in SRFs. If SRRFs are fabricated for traditional small-signal linearization modeling, the physical meaning of the impedance model will become confusing.

The premise that the VSG can actively support the grid is based on the fact that the VSG can operate steadily. In this letter, first, the sequence impedance model of the VSG in SRFs is built by using the harmonic linearization method, and the impedance characteristics of the VSG and the TGCI are compared and analyzed. Then, the influence of different parameters on the stability of the VSG and the TGCI is studied. From a system stability viewpoint, the VSG is shown to be more preferable than the TGCI in an ultraweak grid or in high penetration of renewable energy generation. Finally, the experimental results validate the sequence impedance model and stability analysis.

II. Topology and Control Scheme of the VSG

Fig. 1 shows the topology and control scheme of the VSG [8]. $V_{\rm dc}$ is the dc-side voltage of the VSG, and it can be regarded as a constant value; e_a, e_b, and e_c are the inner electric potentials of the VSG; i_a, i_b, and i_c are the output currents of the VSG; v_a, v_b, and v_c are the output terminal voltages of the VSG; L_f, C_f, and R_f are the filter inductance, filter capacitance, and damping resistance, respectively; L_g and R_g are the equivalent inductance and resistance of the grid, respectively; $R_{\rm line}$ and $L_{\rm line}$ are the resistance and inductance of line between the VSG and the point of common coupling (PCC), respectively; and $Z_{g,p}(s)$ and $Z_{g,n}(s)$ are the positive- and negative-sequence impedances of the grid, respectively. Because the filter capacitance is not included in the VSG control system, it can be considered to be a part of the VSG or a part of the grid for impedance-based stability analysis. For simplifying the analysis, we define $Z_{g,p}(s) = Z_{g,n}(s) = (R_g + sL_g + R_{\rm line} + sL_{\rm line})/(R_f + 1/sC_f)$ for a single VSG connected to the PCC. When multiple VSGs are connected to the PCC, $Z_{g,p}(s) = Z_{g,n}(s) = (R_g + sL_g)$.

The active power controller of the VSG emulates the inertia and primary frequency regulation characteristics of the synchronous generator, and the reactive power controller emulates the primary voltage regulation characteristics of the synchronous generator. According to the instantaneous power theory, the output active power P_e and reactive power Q_e of the VSG can be calculated as follows:

$$\begin{cases} P_e = 1.5(v_\alpha i_\alpha + v_\beta i_\beta) \\ Q_e = 1.5(v_\beta i_\alpha - v_\alpha i_\beta). \end{cases} \tag{1}$$

The modulation wave of the VSG is determined by the active and reactive power controllers as follows:

$$\begin{cases} e_{m,a} = \sqrt{2}E_m \cos\theta \\ e_{m,b} = \sqrt{2}E_m \cos(\theta - 2\pi/3) \\ e_{m,c} = \sqrt{2}E_m \cos(\theta + 2\pi/3) \end{cases}. \tag{2}$$

where E_m and θ are the rms and phase angle of the three-phase modulation wave, respectively.

III. Sequence Impedance Modeling and Impedance Characteristics Analysis of the VSG

The VSG is controlled in SRFs, and therefore, it cannot be modeled in SRFs for traditional small-signal linearization. In this letter, the positive- and negative-sequence output impedance models of the VSG are built by applying the harmonic linearization method. In the time domain, after adding small-signal perturbations, the phase A output voltage and output current of the VSG are as follows:

$$\begin{aligned} v_a(t) &= V_1\cos(2\pi f_1 t) + V_p\cos(2\pi f_p t + \varphi_{v,p}) \\ &\quad + V_n\cos(2\pi f_n t + \varphi_{v,n}) \end{aligned} \tag{3}$$

$$\begin{aligned} i_a(t) &= I_1\cos(2\pi f_1 t + \varphi_{i,1}) + I_p\cos(2\pi f_p t + \varphi_{i,p}) \\ &\quad + I_n\cos(2\pi f_n t + \varphi_{i,n}) \end{aligned} \tag{4}$$

where V_1, V_p, and V_n are the amplitude of the fundamental voltage, positive-sequence voltage perturbation, and negative-sequence voltage perturbation, respectively; I_1, I_p, and I_n are the amplitude of the fundamental current, positive-sequence current response, and negative-sequence current response, respectively; f_1, f_p, and f_n are the fundamental frequency, positive-sequence perturbation frequency, and negative-sequence perturbation frequency, respectively; $\varphi_{v,p}$ and $\varphi_{v,n}$ are the initial phase angle of the positive-sequence and negative-sequence voltage perturbation, respectively; $\varphi_{i,1}$, $\varphi_{i,p}$, and $\varphi_{i,n}$ are the initial phase angle of the fundamental current, positive-sequence current response, and negative-sequence current response, respectively. In the frequency domain, v_a and i_a can be

TABLE I
SYSTEM PARAMETERS OF THE VSG

Parameters	Values	Parameters	Values	Parameters	Values
V_{dc}/V	700	L_{line}/mH	0.024	E_m/V	220
V_{nom}/V	220	R_{line}/Ω	0.05	f_1/Hz	50
L_f/mH	3	P_{set}/kW	10	$f_s(1/T_s)$/kHz	20
C_f/μF	20	Q_{set}/kVar	0	ω_{nom}/(rad/s)	314.159
R_f/Ω	1.5	D_{dam}	5	J/(kg·m²)	0.057
L_g/mH	4	Q_{dam}	321	ω_v/(rad/s)	2π·4000
R_g/Ω	0.2	K	7.1	ω_i/(rad/s)	2π·4000

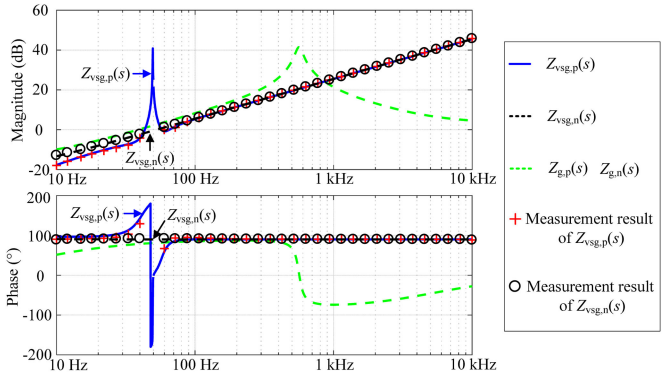

Fig. 2. Sequence impedances of the VSG and their simulation measurement results.

described as follows:

$$v_a[f]=\begin{cases}\mathbf{V}_1, f=\pm f_1\\ \mathbf{V}_p, f=\pm f_p\\ \mathbf{V}_n, f=\pm f_n\end{cases},\quad i_a[f]=\begin{cases}\mathbf{I}_1, f=\pm f_1\\ \mathbf{I}_p, f=\pm f_p\\ \mathbf{I}_n, f=\pm f_n\end{cases} \tag{5}$$

where $\mathbf{V}_1=V_1/2, \mathbf{V}_p=(V_p/2)e^{\pm j\varphi v,p}, \mathbf{V}_n=(V_n/2)e^{\pm j\varphi v,n}$, $\mathbf{I}_1=(I_1/2)e^{\pm j\varphi i,1}$, $\mathbf{I}_p=(I_p/2)e^{\pm j\varphi i,p}$, and $\mathbf{I}_n=(I_n/2)e^{\pm j\varphi i,n}$. The bold capital letters in the formula represent the frequency-domain representation of the signal, including the frequency, amplitude, and phase information of the signal.

From Fig. 1, the relationship among the inner electric potential, output terminal voltage, and output current of the VSG is as follows:

$$L_f\frac{d}{dt}\left[\,i_a\ i_b\ i_c\,\right]^T=\left[\,e_a\ e_b\ e_c\,\right]^T-\left[\,v_a\ v_b\ v_c\,\right]^T. \tag{6}$$

The frequency-domain expressions of the output terminal voltage and output current of the VSG in α–β reference frames can be obtained as follows:

$$v_\alpha[f]=\begin{cases}\mathbf{V}_1, f=\pm f_1\\ \mathbf{V}_p, f=\pm f_p\\ \mathbf{V}_n, f=\pm f_n\end{cases},v_\beta[f]=\begin{cases}\mp j\mathbf{V}_1, f=\pm f_1\\ \mp j\mathbf{V}_p, f=\pm f_p\\ \pm j\mathbf{V}_n, f=\pm f_n\end{cases} \tag{7}$$

$$i_\alpha[f]=\begin{cases}\mathbf{I}_1, f=\pm f_1\\ \mathbf{I}_p, f=\pm f_p\\ \mathbf{I}_n, f=\pm f_n\end{cases},i_\beta[f]=\begin{cases}\mp j\mathbf{I}_1, f=\pm f_1\\ \mp j\mathbf{I}_p, f=\pm f_p\\ \pm j\mathbf{I}_n, f=\pm f_n.\end{cases} \tag{8}$$

By substituting (7) and (8) into (1) and applying the frequency-domain convolution theorem, the expression of the active power in the frequency domain can be obtained as follows:

$$P_e[f]=\begin{cases}3(\mathbf{V}_1\mathbf{I}_1^*+\mathbf{V}_1^*\mathbf{I}_1+\mathbf{V}_p\mathbf{I}_p^*\\ \quad+\mathbf{V}_p^*\mathbf{I}_p+\mathbf{V}_n\mathbf{I}_n^*+\mathbf{V}_n^*\mathbf{I}_n), & \text{dc}\\ 3(\mathbf{V}_1^*\mathbf{I}_p+\mathbf{V}_p\mathbf{I}_1^*), & f=\pm(f_p-f_1)\\ 3(\mathbf{V}_1\mathbf{I}_n+\mathbf{V}_n\mathbf{I}_1), & f=\pm(f_n+f_1)\\ 3(\mathbf{V}_p\mathbf{I}_n+\mathbf{V}_n\mathbf{I}_p), & f=\pm(f_p+f_n)\end{cases} \tag{9}$$

where * denotes complex conjugation.

According to the active power controller of the VSG in Fig. 1, the expression of θ can be obtained as follows:

$$\theta=M(s)(\omega_{\text{nom}}D_{\text{dam}}+P_{\text{set}}/\omega_{\text{nom}}-P_e/\omega_{\text{nom}}) \tag{10}$$

where $M(s)=1/(Js^2+D_{\text{dam}}s)$, J is the virtual moment of inertia, ω_{nom} is the rated angular frequency, D_{dam} is the damping coefficient, and P_{set} is the active power reference.

By substituting (9) into (10) and neglecting terms proportional to second-order perturbations, the expression of θ in the frequency domain is as follows:

$$\theta[f]=\begin{cases}M(s)\left[\omega_{\text{nom}}D_{\text{dam}}+P_{\text{set}}/\omega_{\text{nom}}\right.\\ \quad\left.-3(\mathbf{V}_1\mathbf{I}_1^*+\mathbf{V}_1^*\mathbf{I}_1)/\omega_{\text{nom}}\right], & dc\\ -3M(s)(\mathbf{V}_1^*\mathbf{I}_p+\mathbf{V}_p\mathbf{I}_1^*)/\omega_{\text{nom}}, & f=\pm(f_p-f_1)\\ -3M(s)(\mathbf{V}_1\mathbf{I}_n+\mathbf{V}_n\mathbf{I}_1)/\omega_{\text{nom}}, & f=\pm(f_n+f_1).\end{cases} \tag{11}$$

The phase angle perturbation $\Delta\theta$ is introduced into the phase angle θ of the three-phase modulation wave of the VSG, that is, $\theta=\theta_1+\Delta\theta$, where θ_1 is the phase angle of the fundamental voltage. According to (11), the expression of $\Delta\theta$ in the frequency domain is as follows:

$$\Delta\theta[f]=\begin{cases}-3M(s)(\mathbf{V}_1^*\mathbf{I}_p+\mathbf{V}_p\mathbf{I}_1^*)/\omega_{\text{nom}}, & f=\pm(f_p-f_1)\\ -3M(s)(\mathbf{V}_1\mathbf{I}_n+\mathbf{V}_n\mathbf{I}_1)/\omega_{\text{nom}}, & f=\pm(f_n+f_1).\end{cases} \tag{12}$$

Because $\Delta\theta$ is a small perturbation, $\cos\theta$ can be obtained as

$$\cos\theta=\cos(\theta_1+\Delta\theta)\approx\cos\theta_1-\Delta\theta\sin\theta_1. \tag{13}$$

Based on (12), (13), and the frequency-domain convolution theorem and ignoring the nonlinear coupling at $\pm(f_p-2f_1)$ and $\pm(f_n+2f_1)$, the relationship among the voltage perturbation, current perturbation, and $\cos\theta[f]$ can be expressed as

$$\cos\theta[f]=\begin{cases}-1.5e^{\pm j\varphi_{\text{vir}}}M(s\mp j2\pi f_1)\\ \quad(\mathbf{V}_1^*\mathbf{I}_p+\mathbf{V}_p\mathbf{I}_1^*)/\omega_{\text{nom}}, & f=\pm f_p\\ -1.5e^{\mp j\varphi_{\text{vir}}}M(s\pm j2\pi f_1)\\ \quad(\mathbf{V}_1\mathbf{I}_n+\mathbf{V}_n\mathbf{I}_1)/\omega_{\text{nom}}, & f=\pm f_n\end{cases} \tag{14}$$

where $\varphi_{\text{vir}}=\arcsin(P_e\omega_{\text{nom}}L_f/E_mV_1)+\pi/2$; $\arcsin(P_e\omega_{\text{nom}}L_f/E_mV_1)$ is the power angle of the VSG.

The amplitude of the fundamental wave in $\cos\theta[f]$ is much smaller than the amplitude of the dc component in $\sqrt{2}E_m[f]$ (a difference of two orders of magnitude). Therefore, the output of the reactive power controller of the VSG can be assumed to be constant in the steady state for small-signal modeling. Based on (2) and (14) and considering the influence of the sampling

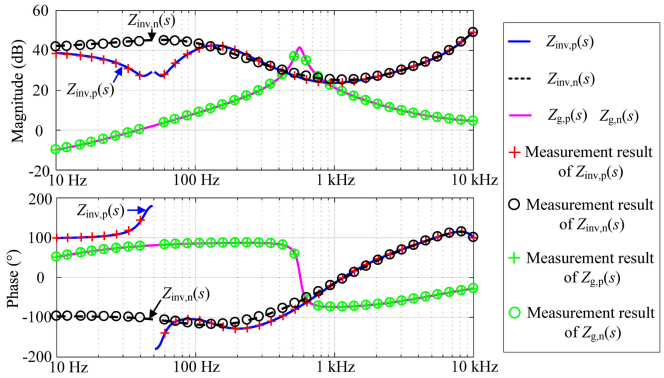

Fig. 3. Sequence impedances of the TGCI and their simulation measurement results.

delay, PWM delay, and low-pass filter, the frequency-domain expression of $e_{m,a}$ can be obtained as follows:

$$e_{m,a}[f] = \begin{cases} -1.5K(s)e^{\pm j\varphi_{\rm vir}}M(s \mp j2\pi f_1) \\ (\mathbf{V}_1^*\mathbf{I}_p + \mathbf{V}_p\mathbf{I}_1^*)/\omega_{\rm nom}, \qquad f = \pm f_p \\ -1.5K(s)e^{\mp j\varphi_{\rm vir}}M(s \pm j2\pi f_1) \\ (\mathbf{V}_1\mathbf{I}_n + \mathbf{V}_n\mathbf{I}_1)/\omega_{\rm nom}, \qquad f = \pm f_n \end{cases} \tag{15}$$

where $K(s) = \sqrt{2}E_m e^{-1.5T_s s}/[(1+s/\omega_v)(1+s/\omega_i)]$; ω_v and ω_i are the cutoff angular frequency of the low-pass filter for the voltage and current signal, respectively; and T_s is the switching period.

By substituting (15) into (6), the positive- and negative-sequence impedances of the VSG can be obtained as follows:

$$Z_{\rm vsg,p}(s) = -\frac{V_p(s)}{I_p(s)} = \frac{0.75V_1M(s-j2\pi f_1)K(s)e^{j\varphi_{\rm vir}}/\omega_{\rm nom} + sL_f}{1+0.75I_1M(s-j2\pi f_1)K(s)e^{j(\varphi_{\rm vir}-\varphi_{i,1})}/\omega_{\rm nom}} \tag{16}$$

$$Z_{\rm vsg,n}(s) = -\frac{V_n(s)}{I_n(s)} = \frac{0.75V_1M(s+j2\pi f_1)K(s)e^{-j\varphi_{\rm vir}}/\omega_{\rm nom} + sL_f}{1+0.75I_1M(s+j2\pi f_1)K(s)e^{j(\varphi_{i,1}-\varphi_{\rm vir})}/\omega_{\rm nom}}. \tag{17}$$

Table I shows the system parameters of the VSG, and the control parameters of the VSG are designed according to [10]. Fig. 2 shows the frequency response characteristics of the positive- and negative-sequence impedances of the VSG and their simulation measurement results. This figure indicates that the impedance measurement results show good agreement with the built impedance model, thus validating the VSG sequence impedance modeling.

The TGCI usually adopts output current feed-forward decoupling control in SRFs [3]; the detailed control block diagram and control parameters are shown in Fig. 11 and Table II in the appendix, respectively. The sequence impedance model of the TGCI was reported in [3]. Fig. 3 shows the frequency response characteristics of the positive- and negative-sequence impedances of the TGCI and their simulation measurement results. In Fig. 3, $Z_{\rm inv,p}(s)$ and $Z_{\rm inv,n}(s)$ are the positive- and negative-sequence impedances of the TGCI, respectively.

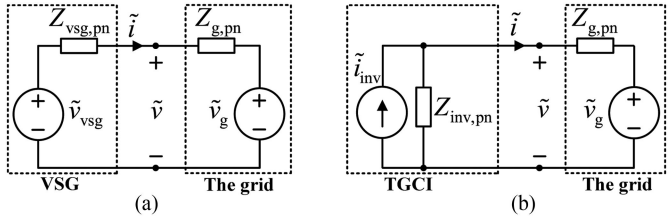

Fig. 4. Small-signal representation of the grid-connected inverter system. (a) Thévenin equivalent circuit of the VSG system. (b) Norton equivalent circuit of the TGCI system.

From Figs. 2 and 3, the sequence impedance characteristics of the VSG and TGCI are compared as follows.

1) In the low- and middle-frequency areas, the impedance amplitude of the VSG is far lower than that of the TGCI. This is because the VSG is controlled as a voltage source, and the equivalent output impedance is small. By contrast, the TGCI is controlled as a current source, and the equivalent output impedance is large.
2) The sequence impedance of the VSG is basically inductive because the VSG has the external characteristics of a synchronous generator. In the low- and middle-frequency areas, the sequence impedance of the VSG is generally consistent with the impedance characteristic of the grid. By contrast, in the middle-frequency area, the sequence impedance of the TGCI is mainly capacitive, making it easy to couple with the grid inductance and thereby cause instability.

IV. Stability Comparison Between the VSG and the TGCI

Fig. 4 shows the small-signal description of the VSG and the TGCI systems. The impedance ratio of the grid-connected inverter system is usually used for the Nyquist stability criterion. The external characteristics of the VSG can be regarded as a voltage source. From Fig. 4(a), the grid-connected current expression of the VSG is as follows:

$$\tilde{i} = \frac{\tilde{v}_{\rm vsg} - \tilde{v}_g}{Z_{\rm vsg,pn} + Z_{g,\rm pn}} = (\tilde{v}_{\rm vsg} - \tilde{v}_g)\frac{1}{Z_{g,\rm pn}}\frac{1}{1 + Z_{\rm vsg,pn}/Z_{g,\rm pn}} \tag{18}$$

where $\tilde{v}_{\rm vsg}$ is the ideal voltage source of the Thévenin equivalent circuit of the VSG, which is stable. The voltage of the ideal grid $\tilde{v}_g$ is also stable. Because the grid admittance acts passively, that is, the real part of the admittance is nonnegative [14], $1/Z_{g,\rm pn}$ is stable. According to (18), whether the VSG-grid system is stable depends on $1/(1 + Z_{\rm vsg,pn}/Z_{g,\rm pn})$.

Therefore, the impedance ratio used to study stability of the VSG is the VSG output impedance divided by the grid impedance, as shown in (19). By contrast, the external characteristics of the TGCI can be regarded as a current source; in this case, the impedance ratio is the grid impedance divided by the

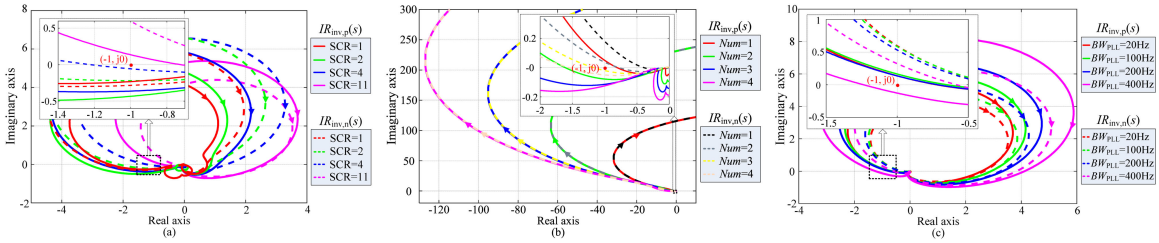

Fig. 5. Nyquist plots of impedance ratios $\mathrm{IR}_{\mathrm{inv},p}(s)$ and $\mathrm{IR}_{\mathrm{inv},n}(s)$ of the TGCI with different parameters. (a) Different SCRs. (b) Different number of paralleled TGCIs. (c) Different PLL bandwidths.

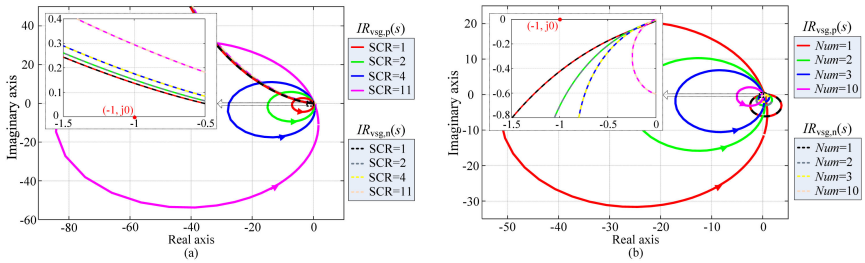

Fig. 6. Nyquist plots of impedance ratios $\mathrm{IR}_{\mathrm{vsg},p}(s)$ and $\mathrm{IR}_{\mathrm{vsg},n}(s)$ of the VSG with different parameters. (a) Different SCRs. (b) Different number of paralleled VSGs.

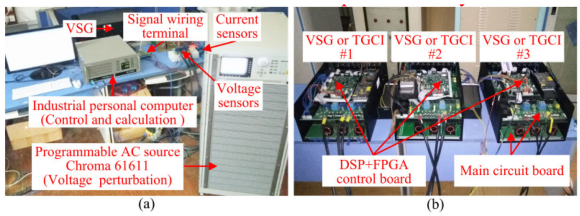

Fig. 7. Experimental platform. (a) Test system for ac impedance measurement. (b) Grid-connected renewable energy generation with three inverters.

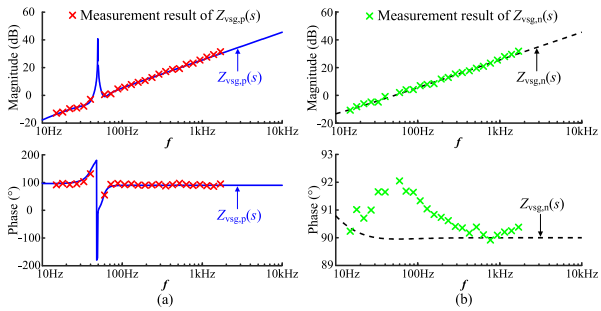

Fig. 8. Experimental results of sequence impedance measurement for the VSG. (a) Measurement results of $Z_{\mathrm{vsg},p}(s)$. (b) Measurement results of $Z_{\mathrm{vsg},n}(s)$.

TGCI output impedance [15], as shown in (20)

$$\begin{aligned} IR_{\mathrm{vsg,p}}(s) &= Z_{\mathrm{vsg,p}}(s)/Z_{g,p}(s), IR_{\mathrm{vsg,n}}(s) \\ &= Z_{\mathrm{vsg,n}}(s)/Z_{g,n}(s) \end{aligned} \tag{19}$$

$$\begin{aligned} IR_{inv,p}(s) &= Z_{g,p}(s)/Z_{inv,p}(s), IR_{inv,n}(s) \\ &= Z_{g,n}(s)/Z_{inv,n}(s). \end{aligned} \tag{20}$$

The grid weakness is distinguished by the short-circuit ratio (SCR), that is, SCR $= S_{\mathrm{SC}}/S_N$, where S_{SC} is the short-circuit capacity at the PCC and S_N is the rated capacity of the grid-connected inverters. In this letter, S_N is 10 kVA, when a single grid-connected inverter is connected to the PCC.

Fig. 5 shows the Nyquist plots of the impedance ratios $\mathrm{IR}_{\mathrm{inv},p}(s)$ and $\mathrm{IR}_{\mathrm{inv},n}(s)$ of the TGCI with different parameters. The poles of $\mathrm{IR}_{\mathrm{inv},p}(s)$ and $\mathrm{IR}_{\mathrm{inv},n}(s)$ are both not in the right half-plane (RHP). In this figure, Num and $\mathrm{BW}_{\mathrm{PLL}}$ represent the number of paralleled TGCIs and the PLL bandwidth, respectively. From Fig. 5(a), when the grid is weaker, the Nyquist plots more easily encircle the critical point $(-1, \mathrm{j}0)$ and the system is more unstable. When SCR ≤ 4, the Nyquist plots encircle $(-1, \mathrm{j}0)$ and the system is unstable. From Fig. 5(b), the Nyquist plot moves toward the left with increasing number of TGCIs, indicating that the system stability deteriorates. When Num ≥ 2, the impedance ratio does not satisfy the Nyquist-stability criterion and the system is unstable. From Fig. 5(c), the PLL bandwidth greatly influences the system stability; specifically, when $\mathrm{BW}_{\mathrm{PLL}}$ increases, the system becomes more unstable, and when $\mathrm{BW}_{\mathrm{PLL}} \geq 400$ Hz, the Nyquist plots encircle $(-1, \mathrm{j}0)$ and the system is unstable.

The analysis in Fig. 5 indicates that the TGCI shows poor adaptability to a weak grid and that the system stability is greatly influenced by the number of paralleled TGCIs and the PLL bandwidth. Therefore, the TGCI is difficult to achieve high penetration renewable energy generation in a weak grid from a system stability viewpoint.

Fig. 6 shows the Nyquist plots of the impedance ratios $\mathrm{IR}_{\mathrm{vsg},p}(s)$ and $\mathrm{IR}_{\mathrm{vsg},n}(s)$ of the VSG with different parameters. $\mathrm{IR}_{\mathrm{vsg},p}(s)$ has two poles in the RHP, and $\mathrm{IR}_{\mathrm{vsg},n}(s)$ has no poles in the RHP. Therefore, when the system is stable, the

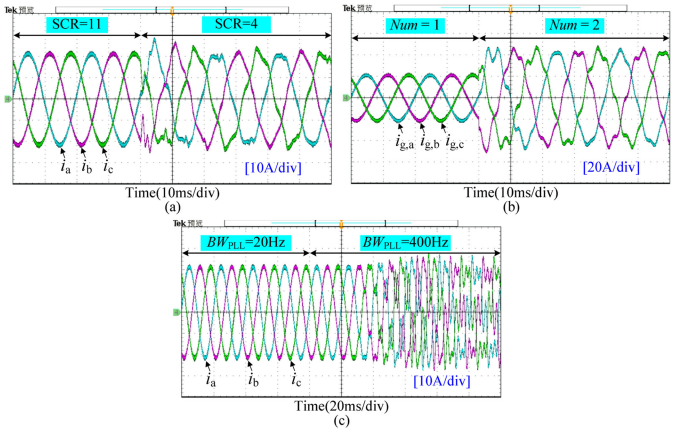

Fig. 9. Experimental results of TGCIs under different conditions. (a) SCR is decreased from 11 to 4. (b) Num is increased from 1 to 2. (c) BW_{PLL} is increased from 20 to 400 Hz.

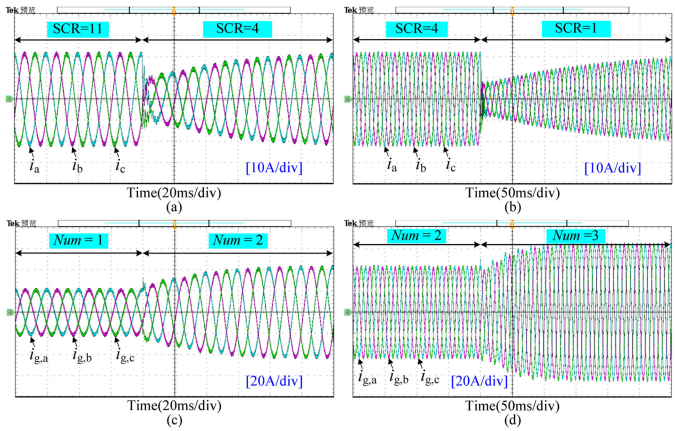

Fig. 10. Experimental results of VSGs under different conditions. (a) SCR is decreased from 11 to 4. (b) SCR is decreased from 4 to 1. (c) Num is increased from 1 to 2. (d) Num is increased from 2 to 3.

Nyquist plots of $IR_{vsg,p}(s)$ should cross the negative real axis at the right side of $(-1, j0)$ once in the counterclockwise direction and those of $IR_{vsg,n}(s)$ cannot encircle $(-1, j0)$. From Fig. 6, irrespective of whether the grid becomes weaker or the number of VSGs increases, the Nyquist plots of $IR_{vsg,p}(s)$ cross the negative real axis at the right side of $(-1, j0)$ once in the counterclockwise direction and those of $IR_{vsg,n}(s)$ do not encircle $(-1, j0)$. Therefore, VSG is more adaptable to a weak grid, and the system remains stable when the VSG penetration is high. In addition, the VSG, such as a synchronous generator, does not need the PLL and consequently cannot be affected by the PLL. Therefore, the VSG can effectively solve stability issues, making it suitable for achieving high penetration of renewable energy generation in an ultraweak grid (SCR $\leq$ 2) from a system stability viewpoint.

V. Experimental Results

To validate the sequence impedance model of the VSG and the stability analysis, experimental platforms for an impedance measurement system and a grid-connected renewable energy generation system are built, as shown in Fig. 7. The impedance measurement system shown in Fig. 7(a) uses a programmable ac source (Chroma 61611) to inject the voltage perturbation. Because of the limit of the output ac voltage frequency and the difficulty in extracting the disturbance signal near the fundamental frequency, the range of impedance measurements in the experiment is 15–45 Hz and 55 Hz to 1.5 kHz. In Fig. 7(b), VSGs and TGCIs share the same hardware circuit. Their control schemes are implemented in TI DSP TMS320F2812. All inverters are connected to the PCC. The experimental parameters are the same as those in the previous analysis.

Fig. 8 shows the experimental results of the sequence impedance measurement for the VSG. These results indicate that the experimental measurement results show good agreement with the built impedance model, thus validating the VSG sequence impedance modeling.

Figs. 9 and 10 show the experimental results of TGCIs and VSGs with different parameters, respectively. When SCR is decreased from 11 to 4, the TGCI oscillates; however, when SCR is further decreased to 1, the VSG still operates stably. When the number of TGCIs is increased from 1 to 2, the system begins to oscillate; however, when the number of VSGs is increased to 3, the VSG does not oscillate. When the PLL bandwidth of the TGCI is increased to 400 Hz, the system oscillates. Therefore, the VSG shows better grid-connected stability than the TGCI.

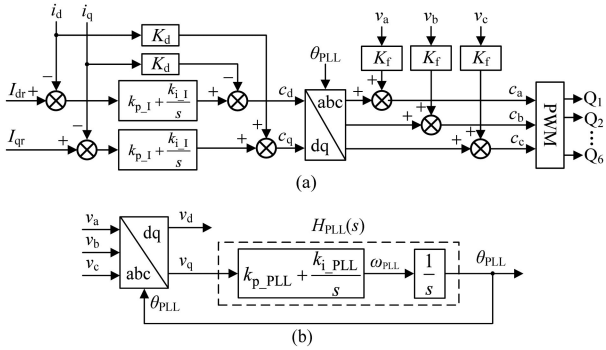

Fig. 11. Control scheme of the TGCI. (a) Output current feed-forward decoupling control. (b) PLL in SRFs.

VI. Conclusion

In this letter, the small-signal sequence impedance model of the VSG is built. By using the impedance-based approach, the grid-connected stability of the VSG and the TGCI is compared. The sequence impedance of the VSG is basically inductive; this is consistent with the impedance characteristics of the inductive grid. Under an ultraweak grid or high penetration of renewable energy generation, the VSG grid-connected system can still run stably without PLL restrictions. From a system stability viewpoint, the VSG is more suitable than the TGCI for achieving high penetration of renewable energy generation in an ultraweak grid.

Appendix

The typical control method of the TGCI is shown in Fig. 11. The control parameters of the TGCI are shown in Table II.

TABLE II
CONTROL PARAMETERS OF THE TGCI

Parameters	Values	Parameters	Values	Parameters	Values
$k_{p\ PLL}$	0.2659	$k_{p\ I}$	0.0343	K_f	0.0029
$k_{i\ PLL}$	10.9988	$k_{i\ I}$	45.7143	K_d	0.0027

REFERENCES

[1] J. Sun *et al.*, "Renewable energy transmission by HVDC across the continent: System challenges and opportunities," *CSEE J. Power Energy Syst.*, vol. 3, no. 4, pp. 353–364, Dec. 2017.

[2] B. Wen, D. Dong, D. Boroyevich, and R. Burgos, "Impedance-based analysis of grid-synchronization stability for three-phase paralleled converters," *IEEE Trans. Power Electron.*, vol. 31, no. 1, pp. 26–38, Jan. 2016.

[3] M. Cespedes and J. Sun, "Impedance modeling and analysis of grid-connected voltage-source converters," *IEEE Trans. Power Electron.*, vol. 29, no. 3, pp. 1254–1261, Mar. 2014.

[4] H. Liu and J. Sun, "Voltage stability and control of offshore wind farms with AC collection and HVDC transmission," *IEEE J. Emerg. Sel. Topics Power Electron.*, vol. 2, no. 4, pp. 1181–1189, Dec. 2014.

[5] K. Alawasa, Y. Mohamed, and W. Xu, "Active mitigation of subsynchronous interactions between PWM voltage-source converters and power networks," *IEEE Trans. Power Electron.*, vol. 29, no. 1, pp. 121–134, Jan. 2014.

[6] K. Alawasa and Y. Mohamed, "Impedance and damping characteristics of grid-connected VSCs with power synchronization control strategy," *IEEE Trans. Power Syst.*, vol. 30, no. 2, pp. 952–961, Mar. 2015.

[7] A. Egea-Alvarez, S. Fekriasl, F. Hassan, and O. Gomis-Bellmunt, "Advanced vector control for voltage source converters connected to weak grids," *IEEE Trans. Power Syst.*, vol. 30, no. 6, pp. 3072–3081, Nov. 2015.

[8] Q. Zhong and G. Weiss, "Synchronverters: Inverters that mimic synchronous generators," *IEEE Trans. Ind. Electron.*, vol. 58, no. 4, pp. 1259–1267, Apr. 2011.

[9] Q. Zhong, "Power-electronics-enabled autonomous power systems: Architecture and technical routes," *IEEE Trans. Ind. Electron.*, vol. 64, no. 7, pp. 5907–5918, Jul. 2017.

[10] H. Wu *et al.*, "Small-signal modeling and parameters design for virtual synchronous generators," *IEEE Trans. Ind. Electron.*, vol. 63, no. 7, pp. 4292–4303, Jul. 2016.

[11] Y. Du, J. M. Guerrero, L. Chang, J. Su, and M. Mao, "Modeling, analysis, and design of a frequency-droop-based virtual synchronous generator for microgrid applications," in *Proc. Annu. Int. Energy Convers. Congr. Exhib. Asia*, Melbourne, Australia, Jun. 2013, pp. 643–649.

[12] S. D'Arco, J. Suul, and O. Fosso, "Small-signal modeling and parametric sensitivity of a virtual synchronous machine," in *Proc. IEEE Power Syst. Comput. Conf.*, Aug. 2014, pp. 1–9.

[13] C. Hu, K. Chen, S. Luo, B. Zhou, and L. Ding, "Small signal modeling and stability analysis of virtual synchronous generators," in *Proc. Int. Conf. Elect. Mach. Syst. Conf.*, Aug. 2017, pp. 1–5.

[14] L. Harnefors, A. Yepes, A. Vidal, and J. Doval-Gandoy, "Passivity-based controller design of grid-connected VSCs for prevention of electrical resonance instability," *IEEE Trans. Ind. Electron.*, vol. 62, no. 2, pp. 702–710, Feb. 2015.

[15] J. Sun, "Impedance-based stability criterion for grid-connected inverters," *IEEE Trans. Power Electron.*, vol. 26, no. 11, pp. 3075–3078, Nov. 2011.